ACS APPLIED ELECTRONIC MATERIALS

pubs.acs.org/acsaelm Article

Domain Dynamics and Local Level Switching Behaviors of Sol–Gel Nanopowder-Derived Lead-Free $Bi_{0.5}(Na_{0.78}K_{0.22})_{0.5}TiO_3$ Ceramics

Sung Sik Won, Jinkee Lee, In-Bo Shim, Angus I. Kingon, and Seung-Hyun Kim*

Cite This: *ACS Appl. Electron. Mater.* 2021, 3, 5641–5650 Read Online

ACCESS | Metrics & More | Article Recommendations | Supporting Information

ABSTRACT: The material properties of sol–gel nanopowder-derived lead-free $Bi_{0.5}(Na_{0.78}K_{0.22})_{0.5}TiO_3$ (BNKT) ceramics are systematically investigated for high-response piezoelectric device applications. To elucidate the principle of the domain dynamics and local level ferroelectric switching behaviors of environmentally friendly BNKT ceramics, we systematically analyze the Rayleigh parameters and the first-order reversal curve (FORC) of the BNKT ceramics and compare the results with those of the standard measurement method. Based on the characterization of Rayleigh parameters, it is clarified that the contribution of the domain-wall motion of the sol–gel-derived BNKT ceramics is higher than that of solid-state reaction-derived ceramics. We also analyze the FORC distribution diagram-associated hysteron density functions for visualizing reversible and irreversible contributions of domain walls and switching behaviors above the Rayleigh regime. The switching behaviors are explained by considering the defects and microstructural differences of the BNKT ceramics, which are affected by both reversible and irreversible contributions. The sol–gel-derived BNKT ceramics show highly localized and well-defined FORC distribution diagrams with the sharp maximum of the irreversible component and the low reversible contribution, which clearly indicate more homogeneous switching properties and less defects than solid-state reaction-derived ceramics because each switching unit gives almost identical contributions to the total polarization. In this study, the developed technique and gained information are used to explore a fundamental understanding of the domain dynamics and local level switching behaviors of lead-free piezoelectric ceramics. We believe that our investigation certainly positions itself in various multifunctional electronic applications without using toxic lead-based piezoelectrics.

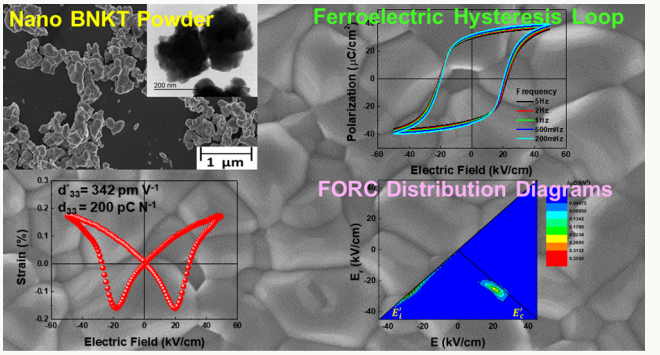

KEYWORDS: *lead-free BNKT ceramics, Rayleigh law, first-order reversal curve (FORC), domain dynamics, local level switching behaviors*

1. INTRODUCTION

Piezoelectric devices are an important part of multitude industries and piezoelectric ceramics are still the largest materials group within that device category. It has experienced healthy growth in the past 20 years even during recent economic downturns and is expected to continue to do so. Traditional application markets are in manufacturing and automotive industries, although lately, the demand has been strongly increased in the medical instruments, information, and telecommunication segments.[1−8] For example, almost every modern cellular phone and laptop computer contain several piezoelectric elements for different functions.

Piezoelectrics have been traditionally dominated by Pb-$(Zr,Ti)O_3$ (PZT)-based materials, which contain ∼60 wt % of environmentally hazardous lead (Pb).[9−13] In several countries, including the European Union (EU) and the U.S. state of California, the Directive Restriction on the Use of Certain Hazardous Substances in Electrical and Electronic Equipment (RoHS) or similar has been implemented in the legislation. According to it, the concentration of toxic lead in homogeneous materials in the household or industrial devices must not exceed 0.1 wt %. Piezoelectric materials for particular applications have been granted an exemption until a feasible alternative for lead-based, specifically PZT-based, materials has been found.[11−13] This caused a huge burst in the research of lead-free materials in the past decade.[11−16]

The material systems that display the highest electromechanical coupling efficiencies are those with a perovskite crystal structure.[14−16] A number of solid solutions have been investigated, and currently, two groups of lead-free piezo-

Received: November 11, 2021
Accepted: December 5, 2021
Published: December 13, 2021

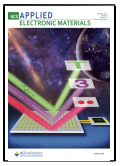

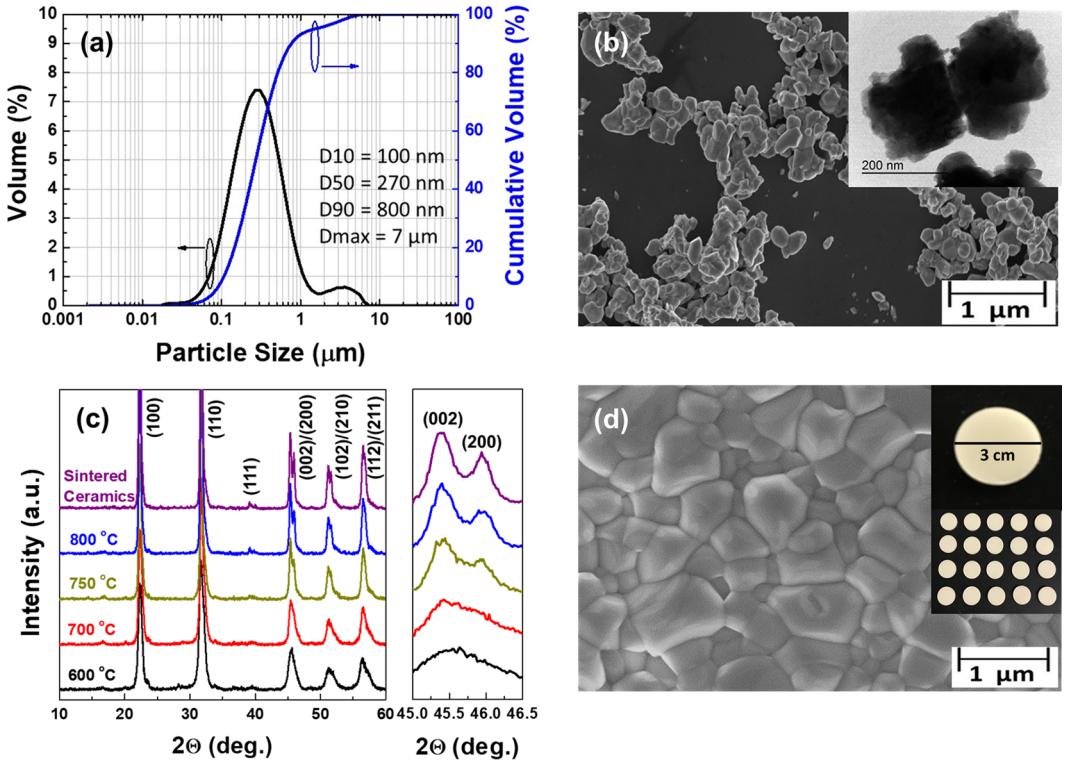

Figure 1. (a) *D*-value analysis showing the size distribution of the BNKT particles. (b) SEM image of the BNKT nanoparticles (inset: highly magnified image). (c) XRD patterns of the dried gel powders calcined at various temperatures from 600 to 800 °C for 2 h and the sintered ceramics at 1100 °C for 2 h. (d) SEM surface image of the sol−gel-derived BNKT ceramic sintered at 1100 °C for 2 h (inset: photographs of the sintered BNKT ceramics).

electric materials are the most attractive: $(K,Na)NbO_3$ (KNN)-based and $(Bi_{1/2}Na_{1/2})TiO_3$-$(Bi_{1/2}K_{1/2})TiO_3$ (BNT-BKT, BNKT)-based perovskites.[11−18] However, piezoelectric properties of pure KNN-based materials without complex multiple dopants (*e.g.*, Li in the A-site and Ta or Sb in the B-site) and specific grain texturing such as *LF4* or *LF4T* are disappointingly low, specifically much inferior large-signal d_{33}* performance,[14,16] which is not suitable for actuator applications. On the contrary, the development of BNKT-based ceramics has progressed to the point that the potential has been demonstrated for the feasibility of environmentally friendly piezoelectric devices.[11,16] However, a large coercive electric field and poor piezoelectric properties due to a non-uniform and porous microstructure have been challenging issues for practical device applications. It is well known that the BNT is a relaxor ferroelectric with a rhombohedral crystal structure at room temperature, while BKT is a ferroelectric with a tetragonal structure. In general, BNT-based ceramics show a porous microstructure, large coercive electric field (E_c ≈ 73 kV/cm), and high leakage current density, which cause insufficient poling, easy breakdown, and poor piezoelectric properties.[19−22] The addition of BKT in the BNT system reduces the coercive field (E_c ≈ 40 kV/cm) and enhances the piezoelectric properties to some extent, but it is still insufficient for practical applications.[23−26] The standard approach to obtain lead-free BNKT materials with good piezoelectric properties has been to follow the example of PZT, for which dielectric permittivity, piezoelectric coefficients, and coupling factor are strongly enhanced in the vicinity of the morphotropic phase boundary (MPB) between the rhombohedral and tetragonal phases. In addition, the properties of piezoelectric BNKT materials strongly depend on the particle size because surface and grain boundary diffusion according to particle size and its distribution affects the densification of ceramics during the high-temperature sintering process. However, conventional solid-state reaction-derived piezoelectric powders generally show an inhomogeneous particle size and large distribution in the range of millimeter or submicrometer scale due to severe agglomeration, which leads to a porous microstructure, cracks, non-uniform composition, and spatial variation of properties in piezoelectric ceramics after sintering.[27−33]

For enhancing dielectric and piezoelectric properties, we selected the 0.78BNT-0.22BKT binary system near MPB as the main lead-free piezoelectric material composition. For the homogeneous particle size and high densification of ceramics, sol−gel-derived powders are used instead of conventional solid-state reaction-derived ones. In contrast to solid-state reaction, the sol−gel process produces nanosized powders with uniform distribution, homogeneous composition control at the molecular level, and high density of sintered ceramics without cracks. For exploring a fundamental understanding of piezoelectric behaviors of lead-free BNKT ceramics, the use of high-quality materials is indispensable. Therefore, we used sol−gel nanopowder-derived reliable quality BNKT ceramics for investigation of the domain states, intrinsic and extrinsic contribution, and piezoelectric properties using Rayleigh-type analysis under subswitching conditions and the first-order reversal curve (FORC) under switching conditions. We believe that the outcome of this research will provide a scientific understanding of the lead-free piezoelectric materials and drop a hint for a significant improvement of the properties, which will hasten the replacement of PZT-based materials in current and future devices by a lead-free alternative.

https://doi.org/10.1021/acsaelm.1c01121
ACS Appl. Electron. Mater. 2021, 3, 5641−5650

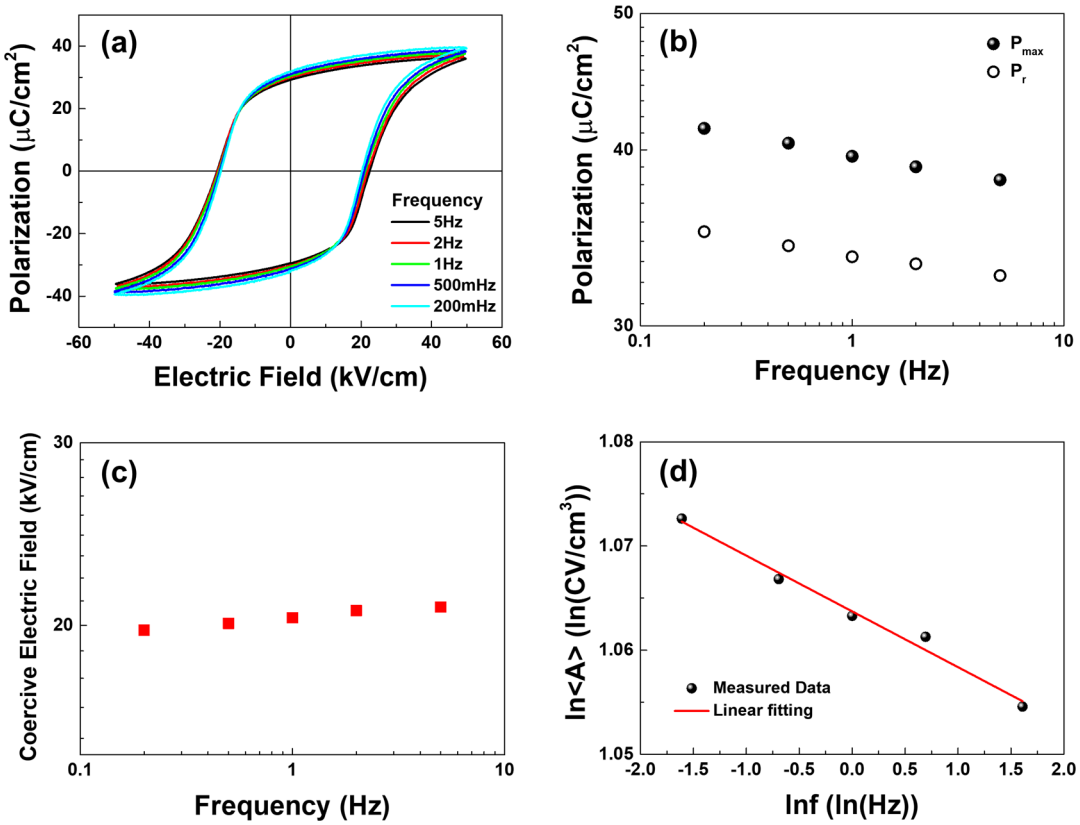

Figure 2. (a) Frequency (f)-dependent P−E hysteresis loops of sol−gel-derived BNKT ceramics. (b) P_{max} and P_r and (c) E_c of sol−gel-derived BNKT ceramics as a function of f. (d) Linear fitting curves of $\ln\langle A\rangle$ as a function of $\ln f$.

2. RESULTS AND DISCUSSION

Figure 1a,b shows the particle size distribution curves and the SEM image of the sol−gel-derived BNKT powders calcined at 800 °C for 2 h. The inset of Figure 1b shows the TEM image of the particles. The D-value analysis is the most widely used method for describing the particle size distributions of synthesized powders.[34] D-values are based on dividing the mass of particles by diameters. The D_{10}, D_{50}, and D_{90} are commonly used to represent the midpoint and range of the particle sizes of a given sample. Particle size distributions have been traditionally calculated based on sieve analysis results, creating an S-curve of cumulative mass retained against the sieve mesh size and calculating the intercepts for 10, 50, and 90% masses. The measured D_{10}, D_{50}, D_{90}, and D_{max} of BNKT powders are 100, 270, 800, and 7 μm, respectively. Since D-values are concerned only with a ratio of masses, a relative mass is sufficient for the analysis, which is not necessary for sample weighing for the measurement. From the D-value analysis, the average particle size of BNKT powders is about 270 nm. In the SEM image, it is found that the powders are composed of polyhedral-shaped particles with some degree of soft agglomeration. The agglomeration of particles can be reduced by the subsequent milling process after calcination. The size of primary particles is also verified using the TEM image, which is well matched with the particle size distribution analysis.

Figure 1c shows XRD patterns of the dried gel powders calcined at various temperatures from 600 to 800 °C for 2 h and the sintered ceramics at 1100 °C for 2 h. A very small pyrochore phase peak is observed at a low calcination temperature of 600 °C, which is assigned to the $Bi_2Ti_2O_7$ structure and completely disappears from 700 °C, followed by a single perovskite phase with no evidence of the second phase. Moreover, in the detailed XRD analysis in the 2θ range of 45.5−47.5°, the XRD patterns clearly show the peak splitting at corresponding angles, indicating the coexistence of rhombohedral and tetragonal phases in BNKT powders calcined over 750 °C. It is well known that BNT has a rhombohedral structure and BKT has a tetragonal structure at room temperature, respectively. The coexistence of rhombohedral (200) and tetragonal (002) in BNKT powders calcined over 750 °C and the sintered ceramics at 1100 °C indicates that the composition of our BNKT $[Bi_{0.5}(Na_{1-x},K_x)_{0.5}TiO_3$, $x = 0.22]$ materials is close to the morphotropic phase boundary (MPB) region. It is interesting to note that an increase in calcination temperatures intensifies the separation of (002) and (200) peaks with an increase in the tetragonality of the BNKT lattice.

Figure 1d shows the SEM surface image of the BNKT ceramic sintered at 1100 °C for 2 h. The sol−gel-derived BNKT ceramic shows a dense and uniform microstructure with well-defined grain boundaries. The dense microstructure may be ascribed to the homogeneous and fine particles in the sol−gel-derived powders.[33] The insets show the photographs of the sintered ceramics with the diameter of 3 cm used in the experiment. All ceramics have crack-free and dense morphologies.

Figure S1a,b shows the SEM images of conventional solid-state reaction-derived BNKT powders calcined at 800 °C for 2 h and the sintered ceramics at 1100 °C for 2 h, respectively. Compared to the sol−gel-derived powders and the sintered ceramics, the particle size of the solid-state reaction-derived

https://doi.org/10.1021/acsaelm.1c01121
ACS Appl. Electron. Mater. 2021, 3, 5641−5650

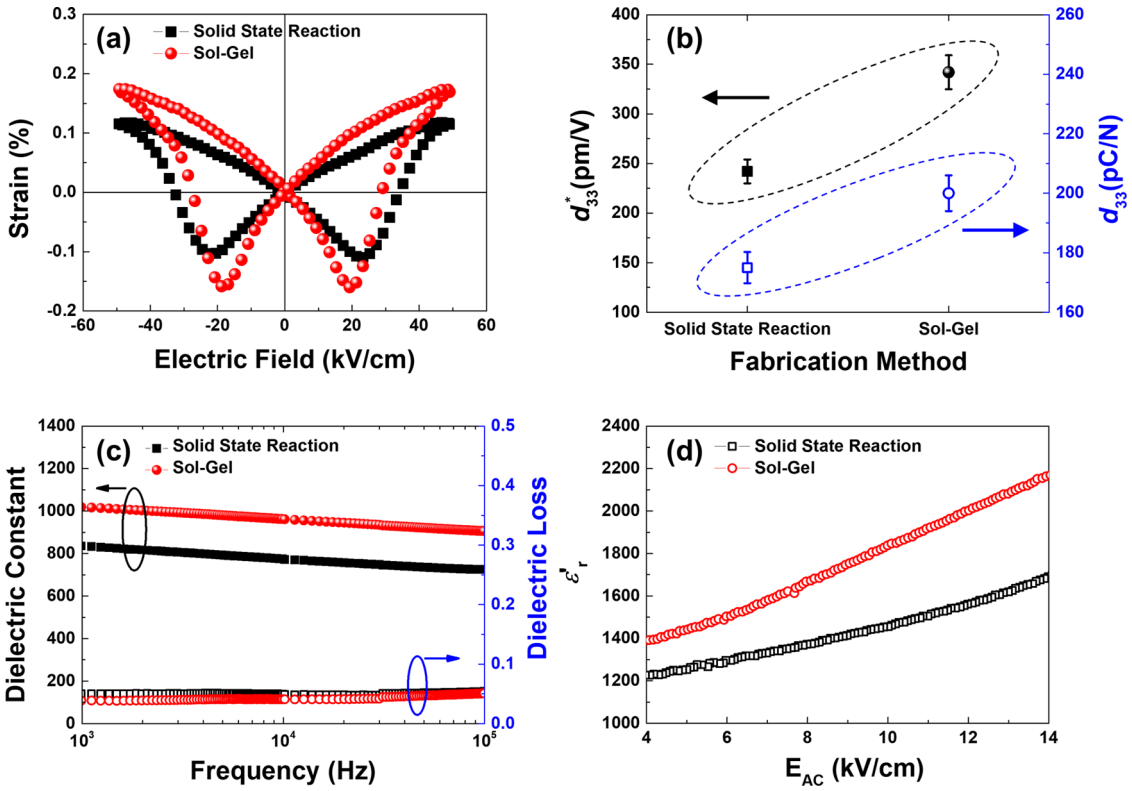

Figure 3. (a) Bipolar strain−electric field (S−E) curves of sol−gel-derived and solid-state reaction-derived BNKT ceramics. (b) Comparison of two types of piezoelectric coupling coefficients between sol−gel-derived and solid-state reaction-derived BNKT ceramics. (c) Frequency-dependent dielectric characteristics of sol−gel-derived and solid-state reaction-derived BNKT ceramics. (d) E_{AC}-dependent relative dielectric permittivity of BNKT ceramics at the frequency of 1 Hz.

powders is less uniform and the density of the ceramics is lower than that of the sol−gel-derived ones.

Figure S2 presents the relative density of the sol−gel-derived BNKT ceramics as a function of sintering temperatures from 1000 to 1200 °C. It is well known that the relative density of the sintered ceramics is directly related to the green density of the pressed ceramic pellets, which is highly dependent on the morphology and uniformity of the initial primary powders. Since our sol−gel-derived powders have the homogeneous and uniform morphology and size distribution, all ceramics using sol−gel-derived powders show the relatively high density over 93%, regardless of the sintering temperature over 1000 °C. The density of BNKT ceramics linearly increases with increasing sintering temperature from 1000 °C to 1150 °C. The maximum density is obtained for the BNKT ceramic sintered at 1150 °C for 2 h, which is around 98.5% of the theoretical density. However, the density becomes lower at higher sintering temperatures than 1150 °C, which might be related to the high volatilization of alkaline elements such as Na and K. It is noted that the density of all BNKT ceramics sintered from 1100 to 1150 °C is similar, which indicates that our sol−gel-derived BNKT ceramics can be fully densified even at the sintering temperature of 1100 °C.

Figure 2a shows the frequency (f)-dependent polarization (P)−electric field (E) hysteresis loops of the sol−gel-derived BNKT ceramics ranging from 200 mHz to 5 Hz under an applied electric field of 50 kV/cm. The ceramics show the well-saturated P−E hysteresis loops with a low coercive electric field (E_c) of 20 kV/cm. It is well known that the P−E hysteresis loops of ferroelectric materials strongly depend on the frequency of the applied electric field. When an alternating current (AC) electric field is applied to a ferroelectric material, the hysteretic polarization reversal process is usually induced by domain-wall motion and domain switching. Without an applied electric field, the free energy of a ferroelectric material prefers the configurations consisting of domains with the same polarization direction. However, with a sufficiently high electric field, the rate of domain nucleation and growth increases. Consequently, the polarization switching and the loop shape are governed by the nucleation and the domain-wall movement, which depend on the experimental conditions such as frequency, applied electric field and temperature, and the microstructure of the material. Therefore, the shape of ferroelectric P−E hysteresis loops is affected by these factors. Specifically, the remnant polarization (P_r) and the E_c are known to have strong frequency dependency.[35−37] It is important to systematically investigate the frequency (f) dependence of P−E hysteresis loops, since it can provide a fundamental understanding on the hysteretic dynamics of domains under an AC electric field.

There have been theoretical and experimental efforts to understand the f dependence of P−E hysteresis loops. To explain the f dependence of hysteresis by using domain dynamics, the Kolmogorov−Avrami−Ishibashi (KAI) model has been commonly used, which is a phenomenological model that considers domain growth as the key process. The empirical relationship between P_r, E_c, and f can be expressed using the KAI model as follows.[38−41]

$$P_r \propto f^{\alpha} \tag{1}$$

$$E_c \propto f^{\beta} \tag{2}$$

https://doi.org/10.1021/acsaelm.1c01121
ACS Appl. Electron. Mater. 2021, 3, 5641−5650

where α and β are the exponential parameters of f for the P_r and E_c, respectively.

Figure 2b shows the maximum polarization (P_{max}) and the P_r of sol−gel-derived BNKT ceramics as a function of f. As the f of the BNKT ceramics increases from 200 mHz to 5 Hz, the P_{max} and P_r increase from 38 $\mu C/cm^2$ to 42 $\mu C/cm^2$ and from 32 $\mu C/cm^2$ to 35 $\mu C/cm^2$, respectively. The exponential parameter (α) of the f for the P_r of the BNKT ceramics is −0.022 based on eq 1.

The f dependence of the E_c is shown in Figure 2c. The exponential parameter (β) of the f for the E_c of the BNKT ceramics is 0.017 based on eq 2. It is interesting to note that there is almost no or negligible f dependence of the E_c, which has a constant value of about 20 kV/cm.

Figure 2d shows the linear fitting curves of $\ln\langle A\rangle$ as a function of $\ln f$ at an applied electric field of 50 kV/cm. The hysterical area $\langle A\rangle$, which shows energy dissipation within one period of polarization reversal, is applied as a characteristic parameter of the dynamic behavior in ferroelectric BNKT ceramic materials. The scaling behavior between $\langle A\rangle$ and f can be described by the following equation.[41,42]

$$\langle A\rangle \propto f^{\gamma} \tag{3}$$

where the exponential parameter (γ) refers to the switching time required by the domain at a given electric field, which is −0.005 based on eq 3.

Figure S3a−d shows the f dependence of $P-E$ hysteresis loops, P_{max}, and P_r, E_c, and the linear fitting curves of $\ln\langle A\rangle$ of the conventional solid-state reaction-derived BNKT ceramics as a function of f for comparison with those of sol−gel nanopowder-derived ceramics. It is clearly demonstrated that the sol−gel nanopowder-derived BNKT ceramics show much less frequency-dependent dynamic properties than the conventional solid-state reaction-derived ceramics. In addition, the E_c and the absolute values of exponential parameters (α, β, and γ) of the sol−gel-derived BNKT ceramics are much smaller than those of solid-state reaction-derived ceramics. These results indicate that the sol−gel-derived BNKT ceramics show faster domain switching at a much lower electric field than conventional solid-state reaction-derived ones.

Figure 3a shows the bipolar strain−electric field ($S-E$) curves of the sol−gel-derived and solid-state reaction-derived BNKT ceramics under an applied frequency of 1 Hz and electric field sweeping of up to 50 kV/cm, respectively. Both BNKT ceramics exhibit a symmetric butterfly-shaped bipolar curve showing the stable ferroelectric and piezoelectric behaviors. However, the sol−gel nanopowder-derived ceramics show much higher positive and negative strains than the conventional solid-state reaction-derived ceramics. The maximum strains of the sol−gel-derived and solid-state reaction-derived BNKT ceramics are 0.17 and 0.12%, respectively.

There are two types of piezoelectric coupling coefficients used in the performance of piezoelectric materials.[43−45] Traditionally, a small-signal d_{33} value has been used to compare the performance of different piezoelectric materials, which is determined by the slope of the strain response at low electric fields when the strain response is still linear. However, for the actuator applications, the achievable strain S_{max} at the applied electric field E_{max} is the key figure of merit, which is measured at high electric fields where the strain-field response deviates from linearity. Their ratio S_{max}/E_{max} (normalized strain, large-signal d_{33}, d_{33}*) is more important than the small-signal d_{33}.[16,46] The large-signal piezoelectric coefficient is conventionally measured by the displacement parallel to the electric field and commonly referred to as d_{33}* when using the Voigt notation.[47,48] The difference between the two is very important and has to be carefully addressed according to applications. In traditional, both small-signal and large-signal responses of "soft" PZT are high and the difference of the two values is similar. Therefore, PZT is the rational choice for universal piezoelectric applications such as sensors, transducers, actuators, and various other piezo-devices. However, as we described previously, the large-signal d_{33}* performance of popular lead-free (K,Na)NbO_3 (KNN)-based materials without multiple dopants and specific grain texturing is very low, which means that the application window of these materials is narrow and may not be suitable for actuator devices.[13,16]

Figure 3b shows a comparison of two types of piezoelectric coupling coefficients between the sol−gel-derived and solid-state reaction-derived BNKT ceramics. The large-signal piezoelectric coefficient d_{33}* of BNKT ceramics is higher than small-signal d_{33}, regardless of fabrication methods of ceramics. The large-signal d_{33}* of the sol−gel-derived BNKT ceramics is calculated as 342 pm/V from the ratio of S_{max}/E_{max} and the small-signal d_{33} is measured as 200 pC/N by a d_{33} meter, which implies that the sol−gel-derived BNKT is a good candidate for both sensors and actuators like PZT-based materials. The solid state-reaction-derived BNKT ceramics show much lower piezoelectric coupling coefficients than the sol−gel-derived ceramics, which are the d_{33}* of 232 pm/V and the d_{33} of 175 pC/N, respectively. This might be a consequence of more uniform and homogeneous grain size and higher densification of the sol−gel nanopowder-derived ceramics than the solid-state reaction-derived ceramics.

Figure 3c shows the frequency-dependent dielectric characteristics of the sol−gel-derived and solid-state reaction-derived BNKT ceramics. As expected, the dielectric permittivity of the sol−gel-derived ceramics with a high density and homogeneous microstructure is higher than that of the solid-state reaction-derived ceramics. The dielectric loss of both ceramics is less than 4%.

In ferroelectric materials such as PZT and BNKT ceramics, most functional properties are strongly influenced by the microstructure, compositional homogeneity, defects, related domain-wall motion, etc. Specifically, piezoelectric and dielectric responses in ferroelectric BNKT ceramics can be divided into two parts, intrinsic and extrinsic properties.[49−51] The "intrinsic" properties are those directly related to the response of the structure at the unit cell level to the imposed conditions. On the other hand, the "extrinsic" contributions, *i.e.*, those related mainly to the motion of domain walls under the imposed conditions, make a major contribution to the properties. Much of the improvement of properties of lead-free piezoelectric materials can be ascribed to the control of the "extrinsic" contributions. It is interesting to note that the domain-wall motion and the domain switching process should involve transgranular cooperation of domains, which means that the quality of grain boundaries, presence of intergranular phase, homogeneous grain size distribution, and density affect domain-wall switching. The movement of domain walls can be achieved by an application of an electric field E. With respect to its magnitude, two regions can be defined: at relatively low to moderate electric fields, the domain-wall motions occur at rather short distances (subswitching conditions), while the nucleation and growth of new domains occur at high electric fields (switching conditions). Note that at room temperature

https://doi.org/10.1021/acsaelm.1c01121
ACS Appl. Electron. Mater. 2021, 3, 5641−5650

and relatively small electric fields, the extrinsic contributions can attribute up to ~75% of the whole macroscopic dielectric and piezoelectric responses and their engineering is of crucial importance for the development of the high-response lead-free piezoelectric materials and devices. However, very limited knowledge exists on extrinsic contributions to dielectric and piezoelectric properties in BNKT-based lead-free ceramic materials, so it is essential to understand these very basic issues.

Generally, the dielectric response (ε') of ferroelectric materials can be expressed by eq 4,[45,49−52]

$$\varepsilon' = \varepsilon'_{\text{int}} + \varepsilon'_{\text{ext}} \tag{4}$$

where $\varepsilon'_{\text{int}}$ is the relative permittivity for the intrinsic contribution and $\varepsilon'_{\text{ext}}$ is that for the extrinsic contribution. Direct evidence of the extrinsic contribution to dielectric properties under subswitching conditions can be observed by measuring dielectric permittivity at different applied AC electric fields (E_{AC}). The E_{AC}-dependent dielectric constant of the ferroelectric materials can be described by the Rayleigh relationship, as shown in eq 5.[45,52−58] Using the Rayleigh law, the reversible and irreversible domain-wall motions of the BNKT ceramics can be characterized, which are described by

$$\varepsilon' = \varepsilon'_{\text{init}} + \alpha' E_{\text{AC}} \tag{5}$$

where $\varepsilon'_{\text{init}}$ is the initial (zero-field) permittivity including contributions from the intrinsic lattice and the reversible extrinsic displacements of the interfaces, while α' is the Rayleigh coefficient and is directly related to the magnitude of the nonlinear response by the irreversible extrinsic displacements.

Figure 3d shows the E_{AC}-dependent relative dielectric permittivity of BNKT ceramics at a frequency of 1 Hz. The reversible and irreversible contributions of domain-wall motion can be analyzed from the results in Figure 3d and eq 5 using the Rayleigh law. The dielectric constant of both ceramics increases with the applied E_{AC}. However, the slope of dielectric permittivity of the sol−gel-derived BNKT ceramics according to E_{AC} is much higher than that of solid-state reaction-derived ceramics, which is mainly due to higher irreversible extrinsic contributions (α'). The reversible and irreversible contributions of both BNKT ceramics are summarized in Table 1. It is

Table 1. Comparison of the Rayleigh Coefficients for the Dielectric Response of BNKT Ceramics

sample	$\varepsilon'_{\text{init}}$	α' (cm/kV)	$\alpha'/\varepsilon'_{\text{init}}$ (cm/kV)
BNKT (solid-state reaction)	900.1	55.4	0.0615
BNKT (sol−gel)	992.0	84.1	0.0848

demonstrated that the Rayleigh parameters of the sol−gel-derived BNKT ceramics are higher than those of the solid-state reaction-derived ones, which implies that the contribution of the domain-wall motion of the sol−gel-derived ceramics is apparently higher than that of the solid-state reaction-derived ceramics.

Measurement of the Rayleigh parameter has been extensively used to investigate domain-wall dynamics in ferroelectric materials. However, it should be noted that the Rayleigh law is only useful when the effects of domain-wall interactions and saturation are negligible, which is the case for the applied electric field below the coercive field (E_c) of less than $1/2E_c$. When higher-order nonlinear terms affect the permittivity at high fields (switching conditions) above the Rayleigh regime, the first-order reversal curve (FORC) is a more powerful tool for investigation of domain switching. The general $P-E$ hysteresis loops are a statistical result of the polarization switching, but the FORC is the deconvolution of the statistical result, which provides the information of local level polarization switching and domain dynamics.[59−62] The FORC is measured using modulated triangle waveforms of each electric field, which starts at a positive saturation field (maximum electric field, E_{max}) and sweeps between the reversal electric field (E_r) and positive saturation, increasing the E_r until it reaches the negative saturated field ($-E_{\text{max}}$), as shown in Figure 4a. In our measurement, the E_{max} is 50 kV/cm, the electric field interval is 200 kV/cm, and the measured frequency is 1 Hz. The inset in Figure 4a represents $P-E$ hysteresis loops of the sol−gel-derived BNKT ceramics corresponding to each reversal electric field during the electric field sweep.

The FORC represents the Preisach density (switching density), *i.e.*, the density distribution of the ideal hysteron, an elementary unit of hysteresis that exhibits a perfect square shape of the $P-E$ hysteresis loop. The Preisach density can be obtained from the FORC using eq 6.

$$\rho^{-}_{\text{FORC}}(E, E_r) = \frac{1}{2}\frac{\partial^2 P^{-}_{\text{FORC}}(E, E_r)}{\partial E_r \partial E} \tag{6}$$

The FORC starting on the descending branch of the main hysteresis loop is denoted as $\rho^{-}_{\text{FORC}}(E, E_r)$ in eq 6, which describes the sensitivity of the polarization with respect to the actual electric field E and the reversal electric field E_r. The FORC distribution diagram-associated hysteron density functions are useful tools for visualizing reversible and irreversible contributions of domain walls and switching behaviors as shown in Figure 4b, which exhibits a contour plot with E and E_r as the horizontal and vertical axes in the distribution diagrams. It should be noted that since the real electric field (E) is always greater than or equal to the reversal electric field (E_r) in the FORC measurement, only the colored area in Figure 4b has a physical meaning. The FORC distribution can be analyzed in terms of the ideal coercive field of the switched hysteron, $E'_c = (E - E_r)/2$, and the internal field, $E'_i = (E + E_r)/2$. When $E = E_r$, it is the E'_c axis, and when $E = -E_r$, it is the E'_i axis. The diagram of the FORC distribution corresponding to the region along the E'_i axis shows the reversible contribution and that along the E'_c axis represents the irreversible contribution.

Figure 4c and Figure S4a show the FORC distribution diagrams for the sol−gel-derived and solid state reaction-derived BNKT ceramics with E_r and E as the vertical and horizontal axes in the same color scale, respectively. The FORC distribution diagrams of both BNKT ceramics have similar shapes and locations of the reversible and irreversible components. The E'_c and E'_i axes are the diagonals of the distribution diagrams, as shown in Figure 4c and Figure S4a. The inset in the upper left shows the main hysteresis loop of each ceramic. The distribution is non-Gaussian, clearly localized, and biased. The reversible and irreversible components can be distinguished using two distinct regions in the FORC distribution diagrams. The reversible component in the diagrams is the region with a strip shape along the E'_i axis, which is defined as eq 7:

https://doi.org/10.1021/acsaelm.1c01121
ACS Appl. Electron. Mater. 2021, 3, 5641−5650

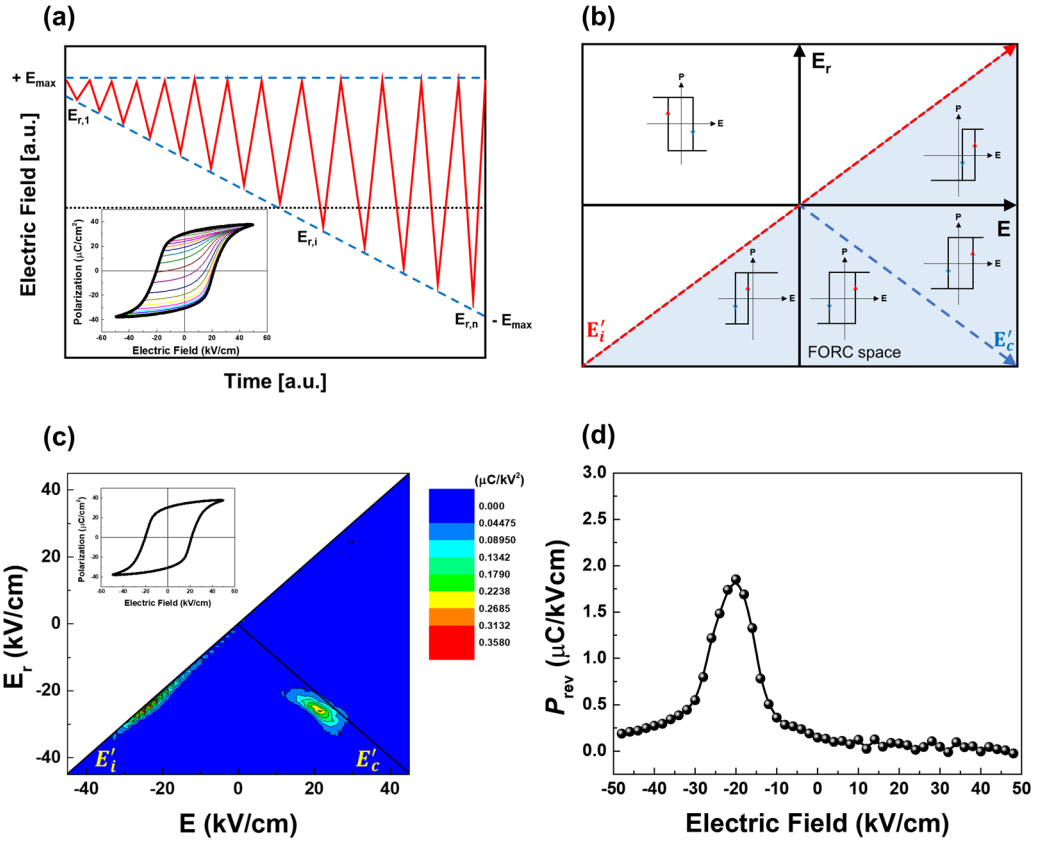

Figure 4. (a) Waveform of the electric field for FORC measurement (inset: measured FORC of sol−gel-derived BNKT ceramics). (b) Sketch of the FORC distribution diagram. (c) FORC distribution diagrams of sol−gel-derived BNKT ceramics (inset: main hysteresis loop). (d) Variation of the reversible distribution (p_{rev}) for the sol−gel-derived BNKT ceramics.

$$p_{rev}(E) = \lim_{E_r \to E-} \frac{1}{2} \frac{\partial P^{-}_{FORC}(E, E_r)}{\partial E_r} \propto \chi \propto \varepsilon_r \tag{7}$$

where χ is the dielectric susceptibility and is proportional to the dielectric constant ε_r. In general, the electric field where the hysteron distribution is maximized in the E'_i axis distribution (reversible hysteron region) coincides with the electric field at the maximum hysteron distribution in the irreversible hysteron region. As shown in eq 7, reversible hysteron affects permittivity. As the applied electric field increases, the density of the reversible hysteron region gradually increases and reaches the maximum near the E'_c, which shows the increase in dielectric constant due to the increased movement of domain walls. Therefore, the maximum permittivity generally appears in the vicinity of the E'_c where most of the domains switch and the material appears to be dielectrically very "soft".

The irreversible contribution is located along the E'_c axis with a contour ridge. The contour ridge represents specific hysterons that can be switched at the applied electric field E. The ideal coercive electric field E'_c of the sol−gel-derived BNKT ceramics is much smaller than that of solid-state reaction-derived ceramics, which is consistent with the result in standard P−E hysteresis measurement. Most hysterons can be switched below E_c. However, for the entire polarization alignment (full switching of all hysterons), it is necessary to apply a bit higher electric field than the E_c from the standard measurement shown in Figure 2a and Figure S3a due to the larger irreversible hysteron region in the FORC diagrams, which implies that the coercive electric field E_c extracted from the standard P−E hysteresis curves does not represent the overall polarization switching of the materials. The E'_c values of the sol−gel-derived and solid-state reaction-derived BNKT ceramics are ∼30 kV/cm (E_c: ∼20 kV/cm) and ∼40 kV/cm (E_c: ∼28 kV/cm for the standard measurement), respectively.

Figure 4d and Figure S4b show the variation of the reversible distribution, p_{rev}, for the sol−gel-derived and solid-state reaction-derived BNKT ceramics, respectively. The maximum values of p_{rev} are 0.356 μC/kV^2 for the sol−gel-derived BNKT ceramics and 0.556 μC/kV^2 for the solid-state reaction-derived ceramics. The calculated ratios ($R_{irre/re}$) of the maximum intensity of the irreversible component over that of the reversible component of the sol−gel-derived and solid state reaction-derived ceramics are 0.803 and 0.505, respectively, which imply that the sol−gel-derived BNKT ceramics have stronger irreversible contribution than the solid-state reaction-derived ceramics. The switching behaviors observed by the FORC distribution diagrams can be explained by considering the defects and microstructural differences of the BNKT ceramics. The ferroelectric switching behaviors are related to domain dynamics such as nucleation and growth of domains and domain-wall motion because the domain structure and its evolution under electric fields are direct consequences of the polarization switching process, which are affected by both reversible and irreversible contributions. Both contributions are strongly dependent on the defects and microstructure of the ceramics. The collective of individual switching units is affected by similar local electric fields under the same boundary conditions. Therefore, less defect ceramics with a more uniform microstructure show more homogeneous switching properties because each unit gives almost identical contribu-

https://doi.org/10.1021/acsaelm.1c01121
ACS Appl. Electron. Mater. 2021, 3, 5641−5650

tions to the total polarization, which is induced to highly localized and well-defined FORC distribution diagrams with the sharp maximum of the irreversible component and the low reversible contribution like the sol−gel-derived BNKT ceramics. On the contrary, the solid-state reaction-derived BNKT ceramics show the broad and dispersed irreversible region in the FORC diagrams, which means that a large number of dipolar units are spread toward higher or lower values of the reversal and actual electric fields due to different local mechanical and electrical boundary conditions. Therefore, the local fields on individual switching units are more dispersed in the FORC diagram because all the units do not equally contribute to the total polarization due to the defective structure, which indicates that the material has more defects or less homogeneous microstructure. In addition, the pinning of the domain wall by such defects makes no further contribution to the irreversible polarization, which shows the low maximum of the irreversible component. If there are lots of pores in the ceramics, uncompensated charges at the ceramic−air interfaces create local depolarizing electric fields and higher electric fields that are necessary to switch the dipolar units than in dense and homogeneous ceramics. The FORC results are in good agreement with the SEM microstructural and standard $P-E$ characteristics of our BNKT ceramics.

It is demonstrated that the FORC approach is one of easy ways to explain the ferroelectric properties and obtain information about the complex ferroelectric physics of the BNKT ceramic at the local level.

3. CONCLUSIONS

This research focused on the use of the emerging collective understanding of the domain dynamics and ferroelectric switching behaviors of environmentally friendly non-lead-based BNKT ceramics and application of this understanding to the enhancement of functional properties that allow the adoption of practical lead-free piezoelectric device applications, with the concomitant positive impact on the environment. We also addressed key solutions about material selection, processing, and performance of lead-free piezoelectric ceramics. We demonstrated the high performance of the BNKT ceramics with a low E_c using sol−gel-derived homogeneous nanopowders for both piezoelectric sensors and actuator applications, which might be due to the uniform microstructure and high density without pores or cracks. There have been theoretical and experimental efforts to understand the materials' behaviors including the reversible and irreversible domain-wall motions and the local level polarization switching process by the analyses of Rayleigh law and FORC distribution diagrams, which make a major contribution to dielectric and piezoelectric properties, and their engineering is very important for the development of the high-response lead-free piezoelectric materials and devices. We also demonstrated that the sol−gel-derived BNKT ceramics have a more homogeneous microstructure and less defects by the characterization of the local field distributions on individual switching units in the FORC diagrams, which enable the ferroelectric switching of the BNKT ceramics at very low electric fields.

Our collective investigations are expected to be integrated to provide a robust knowledge platform to expand the performance and functionality of the environmentally friendly lead-free piezoelectric materials. The platform is also more broadly applicable to various piezoelectric materials and devices with a wide spectrum of application windows excluding the use of toxic lead-based materials.

4. METHODS

4.1. Synthesis of BNKT Powders and Ceramics. Lead-free piezoelectric $Bi_{0.5}(Na_{0.78}K_{0.22})TiO_3$ (BNKT) powders were prepared using a polymeric sol−gel process. High-purity Bi-nitrate pentahydrate [$Bi(NO_3)_3{\cdot}5H_2O$, 98%, Kojundo Chemical Laboratory Co. Ltd., Japan], K-acetate [$K(CH_3COO)$, 99+%, Kojundo Chemical Laboratory Co. Ltd.], Na-ethoxide (C_2H_5ONa, 95%, Kojundo Chemical Laboratory Co. Ltd., Japan), and Ti-butoxide [$Ti(OC_4H_9)_4$, 97%, Kojundo Chemical Laboratory Co. Ltd., Japan] were used as the raw materials. The raw materials were homogeneously mixed in nontoxic butanol (>99.4%, Sigma-Aldrich, USA) as a reactant and solvent instead of the toxic 2-methoxyethanol. For the homogeneous formation of metal−oxygen−metal (M−O−M) bonds at the molecular level in the solution, we used acetylacetone ($C_5H_8O_2$, AcAc, >99.4%, Sigma-Aldrich, USA) as a chelating agent for BNKT solution to reduce the reactivity of the hydrolysis and condensation reactions. Besides chelating effects, AcAc has the good dissolving power for metal salt precursors. To promote the polymerization and gelation, the solvent and the residual organics were slowly removed by heating the solution from 100 to 300 °C with the temperature ramping up rate of 20 °C/h. The resultant gel powders were ground using ball milling for 24 h and then calcined at 800 °C for 2 h. Calcined BNKT powders were pulverized, mixed with an aqueous polyvinyl alcohol (PVA) binder, and pressed into disks of 10 mm in diameter at a uniaxial pressure of 500 kgf/cm^2. The binder was burnt out at 500 °C and the ceramic disks were sintered at 1100 °C for 2 h.

For solid-state reaction-derived BNKT powders, high-purity Bi_2O_3, TiO_2, Na_2CO_3 (99.9%, Kojundo Chemical Laboratory Co. Ltd., Japan), and K_2CO_3 (<99%, Sigma-Aldrich, USA) were used as the raw materials. The raw materials were homogeneously mixed in ethanol with ZrO_2 balls using ball milling for 24 h and then calcined at 800 °C for 2 h. After calcinations, powders were reground and ball-milled for 24 h. The fabrication process of ceramic disks was the same as that of the sol−gel-derived ceramics.

4.2. Characterization. The structural and crystallographic characterization of BNKT powders was investigated using XRD (Bruker Corporation, Billerica, USA) with Cu Kα radiation of 1.54 Å wavelength. The surface morphologies of the BNKT powders and the ceramics were specified by field emission scanning electron microscopy (FE-SEM, JEOL JSM-6700F) and transmission electron microscopy (TEM, JEOL JEM-3000F), respectively.

For electrical measurements, the surfaces of the ceramic disks were screen-printed with silver paste (Silver Conductive Paint, SPI Supplies, USA) and dried for 6 h at 100 °C. Ferroelectric $P-E$ hysteresis loops and the FORC diagram of BNKT ceramics were measured using a Precision Premier II Ferroelectric Tester (Radiant Technologies, USA) with a high-voltage Trek amplifier (10/10, TREK, Inc.). The mechanical strain (S)−electric field (E) curve was measured in a silicon oil bath using a modified Sawyer−Tower circuit and a linear variable differential transducer (LVDT) with a fiber-optic sensor (MTI-2100 Fotonic Sensor, MTI Instruments, Inc., USA). The piezoelectric charge constant of the BNKT ceramics was determined by using a d_{33} meter (YE2730, HAN Tech, Korea). The dielectric constant and tangent loss of the BNKT ceramics were measured using an impedance analyzer (HP4294A, USA) at room temperature. The BNKT ceramics were electrically poled by applying a voltage of 6 kV for 15 min at room temperature.

■ ASSOCIATED CONTENT

Supporting Information

The Supporting Information is available free of charge at https://pubs.acs.org/doi/10.1021/acsaelm.1c01121.

SEM image of conventional solid-state reaction-derived BNKT powders and ceramics (Figure S1); relative density of sol−gel-derived BNKT ceramics as a function

https://doi.org/10.1021/acsaelm.1c01121
ACS Appl. Electron. Mater. 2021, 3, 5641−5650

of sintering temperatures (Figure S2); *P*–*E* hysteresis loop of conventional solid-state reaction-derived BNKT ceramics and analysis (Figure S3); FORC distribution diagrams of conventional solid-state reaction-derived BNKT ceramics (Figure S4) (PDF)

AUTHOR INFORMATION

Corresponding Author

Seung-Hyun Kim − *School of Engineering, Brown University, Providence, Rhode Island 02912, United States;* orcid.org/0000-0003-1202-6606; Email: seunghyun_kim@brown.edu

Authors

Sung Sik Won − *School of Engineering, Brown University, Providence, Rhode Island 02912, United States*

Jinkee Lee − *School of Mechanical Engineering, Sungkyunkwan University, Suwon, Gyeonggi 16419, Korea;* orcid.org/0000-0001-5590-0549

In-Bo Shim − *Department of Nano and Electronic Physics, Kookmin University, Seoul 02720, Korea*

Angus I. Kingon − *School of Engineering, Brown University, Providence, Rhode Island 02912, United States*

Complete contact information is available at: https://pubs.acs.org/10.1021/acsaelm.1c01121

Notes

The authors declare no competing financial interest.

ACKNOWLEDGMENTS

The authors at Brown University would like to thank for the support from National Science Foundation (NSF) under award no. 2044631. J.L. at Sungkyunkwan University was supported by the Korea Environment Industry and Technology Institute (KEITI) grant funded by the Korea Ministry of Environment (MOE) (no. 2019002790003).

REFERENCES

(1) Mohankumar, P.; Ajayan, J.; Yasodharan, R.; Devendran, P.; Sambasivam, R. A Review of Micromachined Sensors for Automotive Applications. *Measurement* **2019**, *140*, 305−322.

(2) Basaeri, H.; Christensen, D. B.; Roundy, S. A Review of Acoustic Power Transfer for Bio-Medical Implants. *Smart Mater. Struct.* **2016**, *25*, 123001.

(3) Pengwang, E.; Rabenorosoa, K.; Rakotondrabe, M.; Andreff, N. Scanning Micromirror Platform Based on MEMS Technology for Medical Application. *Micromachines* **2016**, *7*, 24.

(4) Tian, W.; Ling, Z.; Yu, W.; Shi, J. A Review of MEMS Scale Piezoelectric Energy Harvester. *Appl. Sci.* **2018**, *8*, 645.

(5) Khan, A.; Abas, Z.; Kim, H. S.; Oh, I.-K. Piezoelectric Thin Films: An Integrated Review of Transducers and Energy Harvesting. *Smart Mater. Struct.* **2016**, *25*, No. 053002.

(6) Benoit, R. R.; Rudy, R. Q.; Pulskamp, J. S.; Polcawich, R. G.; Bedair, S. S. Advances in Piezoelectric PZT-Based RF MEMS Components and Systems. *J. Micromech. Microeng.* **2017**, *27*, No. 083002.

(7) Iannacci, J. Internet of Things (IoT); Internet of Everything (IoE); Tactile Internet; 5G − A (Not so Evanescent) Unifying Vision Empowered by EH-MEMS (Energy Harvesting MEMS) and RF-MEMS (Radio Frequency MEMS). *Sens. Actuators A* **2018**, *272*, 187−198.

(8) Muralt, P. Recent Progress in Materials Issues for Piezoelectric MEMS. *J. Am. Ceram. Soc.* **2008**, *91*, 1385−1396.

(9) Yi, L.; Moon, K.; Wong, C. P. Electronics Without Lead. *Science* **2005**, *308*, 1419−1420.

(10) Leontsev, S. O.; Eitel, R. E. Progress in Engineering High Strain Lead-Free Piezoelectric Ceramics. *Sci. Technol. Adv. Mater.* **2010**, *11*, No. 044302.

(11) Hong, C.-H.; Kim, H.-P.; Choi, B.-Y.; Han, H.-S.; Son, J. S.; Ahn, C. W.; Jo, W. Lead-Free Piezoceramics − Where to Move On? *J. Mater.* **2016**, *2*, 1−24.

(12) Rödel, J.; Webber, K. G.; Dittmer, R.; Jo, W.; Kimura, M.; Damjanovic, D. Transferring Lead-Free Piezoelectric Ceramics into Application. *J. Eur. Ceram. Soc.* **2015**, *35*, 1659−1681.

(13) Korujza, J.; Bell, A. J.; Frömling, T.; Webber, K. G.; Wang, K.; Rödel, J. Requirements for The Transfer of Lead-Free Piezoceramics into Application. *J. Materiomics* **2018**, *4*, 13−26.

(14) Shrout, T. R.; Zhang, S. J. Lead-Free Piezoelectric Ceramics: Alternatives for PZT? *J. Electroceram.* **2007**, *19*, 111−124.

(15) Saito, Y.; Takao, H.; Tani, T.; Nonoyama, T.; Takatori, K.; Homma, T.; Nagaya, T.; Nakamura, M. Lead-Free Piezoceramics. *Nature* **2004**, *432*, 84−87.

(16) Hao, J.; Li, W.; Zhai, J.; Chen, H. Progress in High-Strain Perovskite Piezoelectric Ceramics. *Mater. Sci. Eng. R* **2019**, *135*, 1−57.

(17) Aksel, E.; Jones, J. L. Advances in Lead-Free Piezoelectric Materials for Sensors and Actuators. *Sensors* **2010**, *10*, 1935−1954.

(18) Panda, P. K. Review: Environmental Friendly Lead-Free Piezoelectric Materials. *J. Mater. Sci.* **2009**, *44*, 5049−5062.

(19) Hiruma, Y.; Nagata, H.; Takenaka, T. Thermal Depoling Process and Piezoelectric Properties of Bismuth Sodium Titanate Ceramics. *J. Appl. Phys.* **2009**, *105*, No. 084112.

(20) Takenaka, T.; Sakata, K. O.; Toda, K. O. Piezoelectric Properties of $(Bi_{1/2}Na_{1/2})TiO_3$-Based Ceramics. *Ferroelectrics* **1990**, *106*, 375−380.

(21) Tu, C. S.; Siny, I. G.; Schmidt, V. H. Sequence of Dielectric Anomalies and High-Temperature Relaxation Behavior in $Na_{1/2}Bi_{1/2}TiO_3$. *Phys. Rev. B* **1994**, *49*, 11550.

(22) Siny, I. G.; Tu, C. S.; Schmidt, V. H. Critical Acoustic Behavior of The Relaxor Ferroelectric $Na_{1/2}Bi_{1/2}TiO_3$ in The Intertransition Region. *Phys. Rev. B* **1995**, *51*, 5659.

(23) Yoshii, K.; Hiruma, Y.; Nagatha, H.; Takenaka, T. Electrical Properties and Depolarization Temperature of $(Bi_{1/2}Na_{1/2})TiO_3$−$(Bi_{1/2}K_{1/2})TiO_3$ Lead-free Piezoelectric Ceramics. *Jpn. J. Appl. Phys.* **2006**, *45*, 4493−4496.

(24) Elkechai, O.; Manier, M.; Mercurio, J. P. $Na_{0.5}Bi_{0.5}TiO_3$−$K_{0.5}Bi_{0.5}TiO_3$ (NBT-KBT) System: A Structural and Electrical Study. *Phys. Status Solidi A* **1996**, *157*, 499.

(25) Sasaki, A.; Chiba, T.; Mamiya, Y.; Otsuki, E. Dielectric and Piezoelectric Properties of $(Bi_{0.5}Na_{0.5})TiO_3$−$(Bi_{0.5}K_{0.5})TiO_3$ Systems. *Jpn. J. Appl. Phys.* **1999**, *38*, 5564.

(26) Babu, M. V. G.; Kader, S. M. A.; Muneeswaran, M.; Giridharan, N. V.; Padiyan, D. P.; Sundarakannan, B. Enhanced Piezoelectric Constant and Remnant Polarisation in K-Compensated Sodium Potassium Bismuth Titanate. *Mater. Lett.* **2015**, *146*, 81−83.

(27) Hou, Y.; Zhu, M.; Hou, L.; Liu, J.; Tang, J.; Wang, H.; Yan, H. Synthesis and Characterization of Lead-Free $K_{0.5}Bi_{0.5}TiO_3$ Ferroelectrics by Sol−Gel Technique. *J. Cryst. Growth* **2005**, *273*, 500−503.

(28) Hou, Y.; Hou, L.; Zhu, M.; Yan, H. Synthesis of $(K_{0.5}Bi_{0.5})_{0.4}Ba_{0.6}TiO_3$ Nanowires and Ceramics by Sol-Gel−Hydrothermal Method. *Appl. Phys. Lett.* **2006**, *89*, 243114.

(29) Hou, Y.; Hou, L.; Zhu, M.; Wang, H.; Yan, H. Sol−gel Synthesis of Lead-Free $(K_{0.5}Bi_{0.5})_{0.4}Ba_{0.6}TiO_3$ Nanorods. *Mater. Lett.* **2007**, *61*, 3371−3373.

(30) Lidjici, H.; Lagoun, B.; Berrahal, M.; Rguitti, M.; Hentatti, M. A.; Khemakhem, H. XRD, Raman and Electrical Studies on The $(1-x)(Na_{0.5}Bi_{0.5})TiO_3$−$xBaTiO_3$ Lead Free Ceramics. *J. Alloys Compd.* **2015**, *618*, 643−648.

(31) Costa, A. L.; Montanari, G.; Galassi, C.; Cernea, M.; Bezzi, F.; Albonetti, S. Synthesis of Nb Doped Lead Zirconate Titanate by Chemical Methods. *Adv. Eng. Mater.* **2006**, *8*, 572.

(32) Jing, R.; Chen, X.; Ma, J.; Lian, H.; Chen, W. Synthesis, Microstructure, and Electrical Behavior of $(Na_{0.5}Bi_{0.5})_{0.94}Ba_{0.06}TiO_3$ Piezoelectric Ceramics via A Citric Acid Sol−Gel Method. *J. Mater. Sci.* **2018**, *53*, 274−284.

(33) Li, W.; Xu, Z.; Chu, R.; Fu, P.; Zhang, Y. Synthesis and Characterization of $(Na_{0.85}K_{0.15})_{0.5}Bi_{0.5}TiO_3$ Ceramics by Different Methods. *Mater. Res. Bull.* **2011**, *46*, 871−874.
(34) Bowen, P. Particle Size Distribution Measurement from Millimeters to Nanometers and from Rods to Platelets. *J. Disper. Sci. Technol.* **2002**, *23*, 631−662.
(35) Damjanovic, D. Logarithmic Frequency Dependence of The Piezoelectric Effect due to Pinning of Ferroelectric-Ferroelastic Domain Walls. *Phys. Rev. B* **1997**, *55*, R649.
(36) Sivasubramanian, S.; Widom, A.; Srivastava, Y. N. Physical Kinetics of Ferroelectric Hysteresis. *Ferroelectrics* **2004**, *300*, 43−55.
(37) Singh, S. K.; Maruyama, K.; Ishiwara, H. Frequency-Dependent Polarization in $BiFeO_3$ Thin Films. *Integr. Ferroelectr.* **2008**, *97*, 83−89.
(38) Ishibashi, Y.; Orihara, H. A Theory of D-E Hysteresis Loop. *Integr. Ferroelectr.* **1995**, *9*, 57−61.
(39) Ishibashi, Y.; Takagi, Y. Note on Ferroelectric Domain Switching. *J. Phys. Soc. Jpn.* **1971**, *31*, 506−510.
(40) Hu, J.; Hossain, M. E.; Li, J. Investigation on Frequency-Dependent Hysteresis Loops of Ferroelectric Materials. *Smart Mater. Struct.* **2019**, *28*, 125002.
(41) Chen, X.; Dong, X.; Cao, F.; Wang, J.; Wang, G. Field and Frequency Dependence of the Dynamic Hysteresis in Lead Zirconate Titanate Solid Solutions. *J. Am. Ceram. Soc.* **2014**, *97*, 213−219.
(42) Liu, J.-M.; Li, H. P.; Ong, C. K.; Lim, L. C. Frequency Response and Scaling of Hysteresis for Ferroelectric $Pr(Zr_{0.52}Ti_{0.48})O_3$ Thin Films Deposited by Laser Ablation. *J. Appl. Phys.* **1999**, *86*, 5198.
(43) Kerkamm, I.; Hiller, P.; Granzow, T.; Rödel, J. Correlation of Small- and Large-Signal Properties of Lead Zirconate Titanate Multilayer Actuators. *Acta Mater.* **2009**, *57*, 77−86.
(44) Damjanovic, D. Ferroelectric, Dielectric and Piezoelectric Properties of Ferroelectric Thin Films and Ceramics. *Rep. Prog. Phys.* **1998**, *61*, 1267.
(45) Bassiri-Gharb, N.; Fujii, I.; Hong, E.; Trolier-McKinstry, S.; Taylor, D. V.; Damjanovic, D. Domain Wall Contributions to the Properties of Piezoelectric Thin Films. *J. Electroceram.* **2007**, *19*, 49−67.
(46) Jo, W.; Dittmer, R.; Acosta, M.; Zang, J.; Groh, C.; Sapper, E.; Wang, K.; Rödel, J. Giant Electric-Field-Induced Strains in Lead-Free Ceramics for Actuator Applications − Status and Perspective. *J. Electroceram.* **2012**, *29*, 71−93.
(47) Catti, M.; Noel, Y.; Dovesi, R. Full Piezoelectric Tensors of Wurtzite and Zinc Blende ZnO and ZnS by First-Principles Calculations. *J. Phys. Chem. Solids* **2003**, *64*, 2183−2190.
(48) Damjanovic, D.; Budimir, M.; Davis, M.; Setter, N. Piezoelectric Anisotropy: Enhanced Piezoelectric Response along Nonpolar Directions in Perovskite Crystals. *J. Mater. Sci.* **2006**, *41*, 65−76.
(49) Arlt, G.; Dederichs, H.; Herbiet, R. 90°-Domain Wall Relaxation in Tetragonally Distorted Ferroelectric Ceramics. *Ferroelectrics* **1987**, *74*, 37−53.
(50) Herbiet, R.; Robels, U.; Dederichs, H.; Arlt, G. Domain Wall and Volume Contributions to Material Properties of PZT Ceramics. *Ferroelectrics* **1989**, *98*, 107−121.
(51) Robels, U.; Herbiet, R.; Arlt, G. Coupled Losses in PZT near The Morphotropic Phase Boundary. *Ferroelectrics* **1989**, *93*, 95−103.
(52) Won, S. S.; Kawahara, M.; Kim, H.; Lee, J.; Jeong, C. K.; Kingon, A. I.; Kim, S.-H. Nanointerfacial Layer Effect on Dielectric and Piezoelectric Responses in Chemical Solution-Derived Lead-Free Alkaline Niobate-Based Thin Films. *ACS Appl. Mater. Interfaces* **2021**, *13*, 22047−22058.
(53) Zhang, Q. M.; Pan, W. Y.; Jang, S. J.; Cross, L. E. Domain Wall Excitations and Their Contributions to the Weak-Signal Response of Doped Lead Zirconate Titanate Ceramics. *J. Appl. Phys.* **1988**, *64*, 6445.
(54) Taylor, D. V.; Damjanovic, D. Evidence of Domain Wall Contribution to the Dielectric Permittivity in PZT Thin Films at Sub-Switching Fields. *J. Appl. Phys.* **1997**, *82*, 1973.
(55) Taylor, D. V.; Damjanovic, D. Domain Wall Pinning Contribution to the Nonlinear Dielectric Permittivity in Pb(Zr, Ti)O_3 Thin Films. *Appl. Phys. Lett.* **1998**, *73*, 2045.
(56) Damjanovic, D.; Taylor, D. V. Contributions to the Nonlinear Dielectric and Piezoelectric Response of Ferroelectric Thin Films and Ceramics. *Ferroelectrics* **1999**, *221*, 137−146.
(57) Gharb, N. B.; Trolier-McKinstry, S. Dielectric Nonlinearity of $Pb(Yb_{1/2}Nb_{1/2})O_3$−$PbTiO_3$ Thin Films with {100} and {111} Crystallographic Orientation. *J. Appl. Phys.* **2005**, *97*, No. 064106.
(58) Eitel, R.; Randall, C. A. Octahedral Tilt-Suppression of Ferroelectric Domain Wall Dynamics and The Associated Piezoelectric Activity in Pb(Zr,Ti)O_3. *Phys. Rev. B* **2007**, *75*, No. 094106.
(59) Stancu, A.; Ricinschi, D.; Mitoseriu, L.; Postolache, P.; Okuyama, M. First-Order Reversal Curves Diagrams for The Characterization of Ferroelectric Switching. *Appl. Phys. Lett.* **2003**, *83*, 3767.
(60) Goh, Y.; Jeon, S. First-Order Reversal Curve Diagrams for Characterizing Ferroelectricity of $Hf_{0.5}Zr_{0.5}O_2$ Films Grown at Different Rates. *J. Vac. Sci. Technol., B* **2018**, *36*, No. 052204.
(61) Wang, C.; Yang, X.; Wang, Z.; He, C.; Long, X. Investigation of Switching Behavior of Acceptor-Doped Ferroelectric Ceramics. *Acta Mater.* **2019**, *170*, 100−108.
(62) Stoleriu, L.; Stancu, A.; Mitoseriu, L.; Piazza, D.; Galassi, C. Analysis of Switching Properties of Porous Ferroelectric Ceramics by Means of First-Order Reversal Curve Diagrams. *Phys. Rev. B* **2006**, *74*, 174107.

https://doi.org/10.1021/acsaelm.1c01121
ACS Appl. Electron. Mater. 2021, 3, 5641−5650